2024 IEEE/RSJ International Conference on Intelligent Robots and Systems (IROS)
October 14-18, 2024. Abu Dhabi, UAE

Position Control of a Low-Energy C-Core Reluctance Actuator in a Motion System

Mohammad Al Saaideh Yazan M. Al-Rawashdeh Natheer Alatawneh
Khaled Aljanaideh Mohammad Al Janaideh .

Abstract— **This paper introduces a position control system for a motion stage driven by a low-energy C-core reluctance actuator. The central concept explored here is the utilization of a variable air gap to enable energy-efficient operation of the motion stage. First, we show the design and mathematical model of the reluctance-actuated motion system (RAMS). Then, by analyzing open-loop responses of the RAMS under various conditions including variable air gaps and different excitation voltages, we show that using variable air gap can reduce the required current. Finally, the paper formulates a control approach that combines a feedforward controller to linearize the RAMS's dynamic behavior and a state feedback controller to achieve tracking performance. Experimental results demonstrate the effectiveness of this control approach in achieving tracking objectives with errors that are less than 2% for constant desired displacement and less than 10% for tracking a sinusoidal reference signal.**

I. INTRODUCTION

Recent developments in short-stroke motion stages have introduced various reluctance actuators (RAs). These include C-core and E-core reluctance actuators [1]–[5], hybrid-reluctance actuators [6]–[9], and plunger reluctance actuators [10], [11]. Compared to other electromagnetic actuators, reluctance actuators offer higher force density and lower energy dissipation [12]. Consequently, RAs are considered as a promising solution for driving precision motion systems across various applications requiring rapid acceleration. Notable examples include their use in critical applications such as wafer scanners within lithography machines [1] and fast steering mirror systems [9]. However, the widespread adoption of reluctance actuators in high-precision motion systems faces challenges due to the inherent nonlinearities associated with these actuators. These nonlinearities encompass the quadratic relationship between magnetic force and magnetic flux, sensitivity to variations in the air gap [1], [13], and the presence of hysteresis effects in ferromagnetic materials [3], [8]. These complexities present hurdles in designing, modeling, and controlling motion systems incorporating reluctance actuators [14].

M. Al Saaideh and N. Alatawneh are with the Department of Mechanical and Mechatronics Engineering, Memorial University, St. John's, NL A1B 3X5, Canada. (mailsaaideh@mun.ca, nalatawneh@mun.ca)

Y. M. Al-Rawashdeh is with the Electrical Engineering Department at Al-Zaytoonah University of Jordan, 130 Amman, 11733 Jordan (e-mail: yazanmrawashdeh@gmail.com)

K. Aljanaideh is with the Department of Aeronautical Engineering, Jordan University of Science and Technology, Irbid 22110, Jordan (kfaljanaideh@just.edu.jo).

M. Al Janaideh is with School of Engineering, University of Guelph, Guelph, ON N1G 2W1, Canada (maljanai@uoguelph.ca).

In the last decade, several research endeavours have emerged intending to advance reluctance actuators for precision motion systems. These studies mainly focus on developing a control system that can linearize the dynamic behavior of the reluctance actuator under variation in the air gap. In [1], a flux-based control approach is presented to linearize the short-stroke reluctance actuator and reduce the actuator's stiffness. This approach combines two feedback control loops; an inner control loop and an outer control loop. The inner control loop aims to achieve a desired reference voltage using the sensing coil for voltage measurements. The outer control loop uses a simple low-bandwidth proportional-integral (PI) controller for drift stabilizing. This approach is tested for static air gaps in the $[0.7,\ 1.1]$ mm range. In [2], the Preisach model was used to describe the magnetic hysteresis nonlinearities of a reluctance actuator with a fixed air gap of 0.5 mm and an air-gap variation in the range of μm. This approach presents a flux estimator designed by implementing an observer based on the electromagnetic model of the reluctance actuator. In [3], the Chua model and the Prandtl-Ishlinskii model were combined as the two-stage model to characterize the rate-dependent hysteresis nonlinearities of the reluctance actuator with a fixed air gap of 0.5 mm. This model implements the inverse of the hysteresis model as a feedforward compensator of the hysteresis nonlinearity. Recently, a new type of actuator called the hybrid-reluctance actuator has been developed for micropositioning stages, which combines a reluctance actuator with an extra permanent magnet on the mover. This innovation has been demonstrated in several studies found in the literature, including [7], [8], [15]–[19].

II. MAIN CONTRIBUTIONS AND COMPARISON WITH LITERATURE

Previous research, as demonstrated in studies like [1]–[3], primarily concentrated on developing control systems for reluctance actuators featuring fixed air gaps. Furthermore, these investigations did not address the integration of these actuators into motion systems, wherein the mover is an inherent component of the movable stage. Furthermore, the hybrid-reluctance actuator, as introduced in [8], [17]–[19], has a noteworthy limitation. Its use of permanent magnets can result in performance degradation caused by demagnetization effects, ultimately reducing the actuator's output force and efficiency over time. Moreover, including permanent magnets in a hybrid reluctance actuator may result in higher manufacturing expenses and pose challenges compared to

979-8-3503-7769-9/24/$31.00 ©2024 IEEE

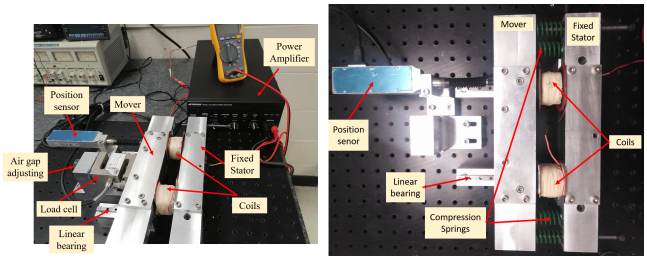

(a) (b)

Fig. 1: The Reluctance-actuated motion system (RAMS) (a) the experimental setup of the system and (b) the configuration using four compression springs.

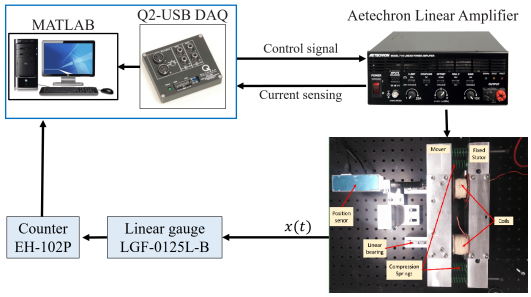

Fig. 2: The block diagram representation of the experimental setup for the reluctance-actuated motion system (RAMS).

other types of reluctance actuators. In particular, the main contributions of the paper can be summarized as:

- Designing a low-energy reluctance actuator with a variable air gap between the mover and the stator of the actuator.
- Characterization of the low-energy reluctance actuator by analyzing its steady-state characteristics under different applied voltages, air gaps, and mechanical stiffness of the motion state.
- Developing a control system that combines a feedforward controller to linearize the dynamic behavior of the RAMS and a state feedback controller to achieve position-tracking objectives.

III. System Description and Dynamic Modeling

This section introduces the proposed Reluctance-Actuated Motion System (RAMS) design and outlines the experimental setup. Next, we will develop a dynamic model taking into account the lumped parameter model of the RAMS.

A. System Description

Figure 1(a) shows the design of the proposed RAMS, which features a motion stage propelled by a C-core reluctance actuator. The reluctance actuator comprises two essential components: A C-core stator and an I-core mover. The stator and the mover are constructed using laminations made from Nonoriented Electrical Steel (M-19), with each lamination having a thickness of 0.35 mm. These laminations are meticulously stacked to form a cross-sectional area measuring 25×25 mm^2. The entire assembly of the C-core and I-core is enclosed within a robust aluminum structure, providing structural support and securing the laminations in place. Furthermore, on each limb of the C-core, there are two excitation coils, each comprising 120 turns. These coils provide the necessary magnetic flux to operate the reluctance actuator.

The mover is housed within an aluminum structure, which serves as the motion stage for the entire system and possesses a total mass of 1.65 kg. The system incorporates compression springs (ISO D DIE SPRING). These springs are strategically placed between a fixed point and the motion stage, as depicted in Figure1(b). They are enclosed within spring housings and collectively provide a restraining mechanism.

B. Experimental setup

Figure 2 presents a block diagram representation of the experimental setup for RAMS. The experimental setup includes an AC/DC linear voltage amplifier (AE Techron 7118) that powers the reluctance actuator's excitation coils. This versatile amplifier offers a power output of 425 VA, adjustable current from 1 A to 25 A, and a voltage range of ± 150 V. A linear gauge (LGF-125L-B from Mitutoyo) with a 25 mm measurement range and 1 µm resolution is employed to track the motion stage's position. A linear digital gauge counter (EH-10P from Mitutoyo) collects data from the linear gauge and outputs measurements in the +1 V to +4 V with an accuracy of $\pm 1\%$. A data acquisition card (Q2-USB) equipped with a 12-bit A/D and D/A converter captures force and displacement data and applies voltage control signals to the linear amplifier.

C. Dynamic model

The dynamic model of the RAMS is formulated to describe the interaction among electrical, magnetic, and mechanical behavior as described in [20]. Define the states of the system as the displacement $x_1 = x$, the velocity $x_2 = \dot{x}$, and the magnetic flux B, then the dynamic model of the RAMS is given by

$$\dot{x}_1 = x_2, \tag{1}$$

$$\dot{x}_2 = -\frac{k}{m}x_1 - \frac{b}{m}x_2 + \frac{1}{m}F, \tag{2}$$

$$\dot{B} = -\alpha(g_o - x_1)B + \psi + \frac{1}{N\mathcal{A}_c}u, \tag{3}$$

$$F = \frac{\mathcal{A}_c}{\mu_o}B^2, \tag{4}$$

$$y = x_1, \tag{5}$$

where y is the output of the system, $\psi \triangleq -\frac{l_c}{N^2\mathcal{A}_c}H_f$ is an unknown nonlinear function that represents the magnetic field H_f in the reluctance actuator related to the magnetic hysteresis nonlinearities, and $\alpha \triangleq \frac{2R}{\mu_o N^2 \mathcal{A}_c}$ is a positive constant related to the system's parameters.

IV. System Characterization and Open-Loop Response

This section is dedicated to the experimental characterization of the RAMS. The primary objective is to obtain the output displacement in an open-loop configuration under a specified voltage input (u). In experiments characterization,

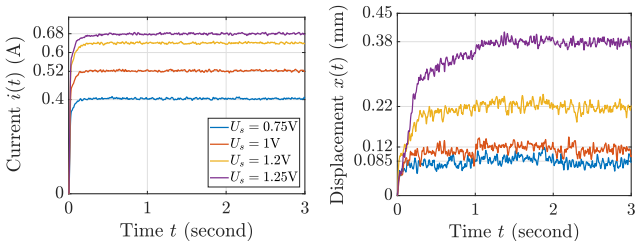

(a) (b)

Fig. 3: The time response of the RAMS with stiffness $k = 50$ N/mm and nominal air gap of $g_o = 1$ mm (a) the measured current i in A; and (b) the measured displacement x in mm.

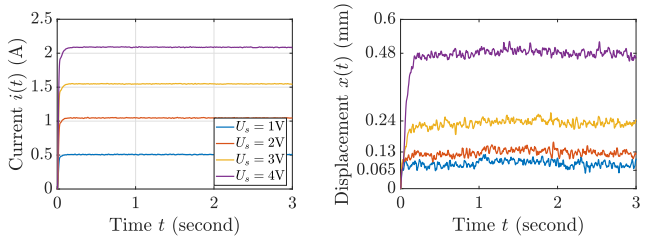

(a) (b)

Fig. 4: Time response of the RAMS with a stiffness of $k = 50$ N/mm and a nominal air gap of $g_o = 2$ mm (a) the measured current i in A; and (b) the measured displacement x in mm.

the compression springs are considered with equivalent stiffness coefficients of $k \in \{50,\ 100\}$ N/mm, and the nominal air gap values are $g_o = \in \{1,\ 2\}$ mm.

A. Time response for the RAMS with two compression springs

In this experiment, the RAMS is utilized with two compression springs, collectively contributing to a total stiffness of approximately $k = 50$ N/mm. The chosen range of applied voltage is carefully determined to ensure stable operation, preventing any contact between the mover and the C-core stator. Figure 3 displays the time response of the measured current and displacement for various constant voltage inputs: $u = U_s \in \{0.75, 1, 1.2, 1.25\}$ V, with a nominal air gap of $g_o = 1$ mm. Conversely, Figure 4 illustrates the time response under different constant voltage inputs: $u = U_s \in \{1, 2, 3, 4\}$ V, with a nominal air gap of $g_o = 2$ mm.

The steady-state values for the measured current and displacement derived from Figure 4 are summarized in Table I. Accordingly, it can be observed that the system requires less input current for the smaller air gap of $g_o = 1$ mm compared to the larger air gap of $g_o = 2$ mm. To illustrate, for $g_o = 1$ mm, maintaining a stable displacement of approximately $x_{ss} = 0.2$ mm requires an input current of $i = 0.61$ A, resulting in power consumption of $P = 0.732$ W. Conversely, for $g_o = 2$ mm, achieving the same displacement demands an input current of $i = 1.55$ A, resulting in power consumption of $P = 4.65$ W. Consequently, the RAMS displays enhanced power efficiency for smaller nominal air gaps.

TABLE I: The steady-state value of the measured current and displacement for the RAMS with a stiffness of $k = 50$ (N/mm)

	Nominal air gap $g_o = 1$ (mm)	
Applied voltage $u = U_s$(V)	**Displacement x_{ss} (mm)**	**Current i_{ss} (A)**
0.75	0.0878	0.4
1	0.1186	0.5224
1.2	0.2232	0.6045
1.25	0.3818	0.6797
	Nominal air gap $g_o = 2$ (mm)	
Applied voltage $u = U_s$(V)	**Displacement x_{ss} (mm)**	**Current i_{ss} (A)**
1	0.092	0.508
2	0.1329	1.0463
3	0.238	1.5485
4	0.4846	2.0879

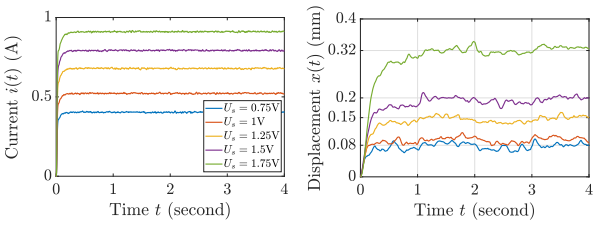

(a) (b)

Fig. 5: Time response of the RAMS with a stiffness of $k = 100$ N/mm and a nominal air gap of $g_o = 1$ mm (a) the measured current i in A; and (b) the measured displacement x in mm.

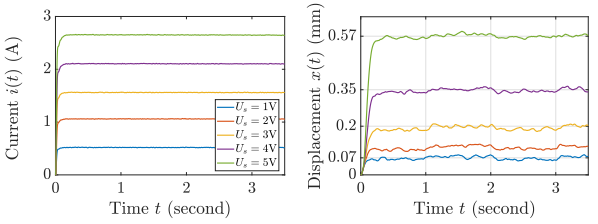

(a) (b)

Fig. 6: Time response of the RAMS with a stiffness of $k = 100$ N/mm and nominal air gap of $g_o = 2$ mm (a) the measured current i in A; and (b) the measured displacement x in mm.

B. Time response for the RAMS with four compression springs

In this experiment, the RAMS is configured with four compression springs with a total system stiffness of about $k = 100$ N/mm. The behavior of the system can be observed in Figure 5, which shows the time response of measured current and displacement under various constant voltage inputs: $u = U_s \in \{0.75, 1, 1.25, 1.5, 1.75\}$ V for a nominal air gap of $g_o = 1$ mm. Conversely, Figure 6 demonstrates the time response under various constant voltage inputs: $u = U_s \in \{1, 2, 3, 4, 5\}$ V at a nominal air gap of $g_o = 2$ mm. Table II summarizes the steady-state values of the measured current and displacement illustrated in Figure 5. Compared with Table I, note that the reluctance actuator

TABLE II: Steady-state values of the measured current and displacement for the RAMS with the a stiffness of $k = 100$ N/mm.

	Nominal air gap $g_o = 1$ (mm)	
Applied voltage $u = U_s$(V)	**Displacement x_{ss} (mm)**	**Current i_{ss} (A)**
0.75	0.0785	0.4
1	0.0946	0.522
1.25	0.1457	0.6789
1.5	0.1946	0.7928
1.75	0.3206	0.9108
	Nominal air gap $g_o = 2$ (mm)	
Applied voltage $u = U_s$(V)	**Displacement x_{ss} (mm)**	**Current i_{ss} (A)**
1	0.071	0.518
2	0.1143	1.06
3	0.195	1.56
4	0.349	2.10
5	0.5719	2.65

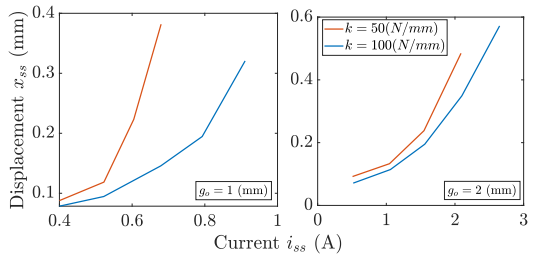

Fig. 7: Current-displacement characteristic of the RAMS with $k = 50$ N/mm and $k = 100$ N/mm and air gap values of $g_o = 1$ mm (left) and $g_o = 2$ mm (right).

demands a higher input current to generate a larger force, aiming to counterbalance the rise in restraining force caused by higher stiffness (k) as shown by the current-displacement characteristic in Figure 7. As observed in Section IV-A, for $g_o = 2$ mm, maintaining a stable displacement of approximately $x_{ss} = 0.2$ mm requires an input current of $i = 0.793$ A, resulting in power consumption of $P = 1.2$ W. Conversely, for $g_o = 2$ mm, achieving the same displacement demands an input current of $i = 1.56$ A, resulting in power consumption of $P = 4.68$ W. Consequently, the RAMS displays enhanced power efficiency for smaller nominal air gaps.

V. Position Tracking Control Design

Characterizing the RAMS under different conditions shows a nonlinear behavior of the force and the output displacement. This section presents a feedforward controller for the RAMS to linearize the reluctance actuator's dynamic behaviour. The feedforward controller is designed using the perturbation theory as follows.

A. Feedforward controller

The dynamic model of the reluctance actuator is given by (3). Assuming a small constant $\epsilon \triangleq \mu_o \mathcal{A}_c$, and using a perturbation approach, (3) can be written as

$$\epsilon \dot{B} = -\frac{2R}{N^2}(g_o - x_1)B + \epsilon\psi + \frac{\mu_o}{N}u, \tag{6}$$

where $\mu_o = 4\pi \times 10^{-7}$ H/m and $\mathcal{A}_c$ represent the cross-section of the C-core. Assuming that $\epsilon \ll 1$, then (6) can be approximated as

$$B \approx \frac{N\mu_o}{2R}\frac{1}{(g_o - x_1)}u. \tag{7}$$

Now, consider a desired magnetic force F_d such as the magnetic flux B_d can be defined as $B_d \triangleq \sqrt{\frac{\mu_o}{\mathcal{A}_c}F_d}$. Then, using (7), the feedforward control law can be expressed as

$$u_{FF} \approx \frac{2R}{N\mu_o}(g_o - x_1)B_d. \tag{8}$$

The proposed feedforward control law (8) is used to drive the RAMS in an open-loop configuration, as shown in Figure 8.

Applying the control law (8) into (3) yields

$$\dot{B} \approx -\frac{2R}{\mu_o N^2 \mathcal{A}_c}(g_o - x_1)B + \psi + \frac{2R}{N^2\mu_o\mathcal{A}_c}(g_o - x_1)B_d. \tag{9}$$

Consider the error of the magnetic flux defined by

$$e_B = B_d - B, \tag{10}$$

where B is the actual magnetic flux, then taking the derivative of (10) and using (9) yields

$$\dot{e}_B = \frac{2R}{\mu_o N^2 \mathcal{A}_c}(g_o - x_1)e_B + \psi - \dot{B}_d, \tag{11}$$

where $\dot{B}_d = \frac{1}{2}\sqrt{\frac{\mu_o}{\mathcal{A}_c F d}}$.

Next, consider the error in the magnetic force defined by $e_F = F_d - F$. Then, using (4), we have

$$e_F = 2e_B\sqrt{\frac{\mathcal{A}_c}{\mu_o}F_d} + \frac{\mathcal{A}_c}{\mu_o}(e_B)^2. \tag{12}$$

Thus, under the feedforward control law (8), the dynamic of RAMS (1)–(4) can be expressed as

$$\dot{x}_1 = x_2, \tag{13}$$

$$\dot{x}_2 = -\frac{k}{m}x_1 - \frac{b}{m}x_2 + \frac{1}{m}F_d + \frac{1}{m}e_F, \tag{14}$$

$$\dot{e}_B = \frac{2R}{\mu_o N^2 \mathcal{A}_c}(g_o - x_1)e_B + \psi - \frac{1}{2}\sqrt{\frac{\mu_o}{\mathcal{A}_c F d}}, \tag{15}$$

$$e_F = 2e_B\sqrt{\frac{\mathcal{A}_c}{\mu_o}F_d} + \frac{\mathcal{A}_c}{\mu_o}(e_B)^2 \tag{16}$$

B. State Feedback Controller

In the previous section, the feedforward controller is proposed to linearize the dynamic behavior of the reluctance actuator, so the relationship between the desired force F_d and the output displacement x is linear. The state feedback controller that has been designed is seamlessly incorporated with the feedforward controller, as depicted in Figure 8.

The dynamic model of the RAMS under the feedforward controller is presented by

$$\dot{x}_1 = x_2, \tag{17}$$

$$\dot{x}_2 = -\frac{k}{m}x_1 - \frac{b}{m}x_2 + \frac{1}{m}F_d + \frac{1}{m}e_F, \tag{18}$$

where F_d the control input and e_F is the unknown feedforward error.

Next, we introduce the design of a state feedback controller to determine the desired force F_d to track a desired position of the motion system. We assume that all states (x_1, x_2) are available for feedback and the force error due to the feedforward controller e_F is bounded. The full-state feedback control is designed based on the backstepping

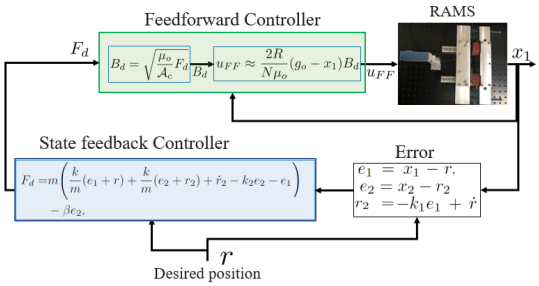

Fig. 8: The feedforward and state feedback controllers structure for the reluctance-actuated motion system (RAMS).

procedure for systems represented in the strict-feedback form [21].

Consider a tracking error defined as $e_1 = x_1 - r$, $e_2 = x_2 - r_2$, where r is the desired position with bounded derivatives, and r_2 is a desired signal selected as $r_2 = -k_1 e_1 + \dot{r}$, where k_1 is a designed positive parameter. Then, (17)–(18) transform into the error dynamics given by

$$\dot{e}_1 = -k_1 e_1 + e_2, \tag{19}$$

$$\dot{e}_2 = -\frac{k}{m}(e_1 + r) - \frac{b}{m}(e_2 + r_2) - \dot{r}_2 + \frac{1}{m}F_d + \frac{1}{m}e_F. \tag{20}$$

We need to design a state feedback controller to make the origin of the (19), (20) exponentially stable, hence achieving the desired tracking goal. For this purpose, consider a smooth and positive definite Lyapunov function candidate as

$$V_a = \frac{1}{2}e_1^2 + \frac{1}{2}e_2^2. \tag{21}$$

Setting $F_d \triangleq \Gamma(e_1, e_2, r_2)$ as

$$F_d = m\left(\frac{k}{m}(e_1 + r) + \frac{k}{m}(e_2 + r_2) + \dot{r}_2 - k_2 e_2 - e_1\right) - \beta e_2, \tag{22}$$

where $\dot{r}_2 = -k_1\dot{e}_1 + \ddot{r}$ and k_2 is a designed positive parameter, (19)-(20) can be written as

$$\begin{bmatrix}\dot{e}_1 \\ \dot{e}_2\end{bmatrix} = A_1 e_a + \begin{bmatrix}0 \\ \frac{1}{m}\end{bmatrix}(e_F - \beta e_2), \tag{23}$$

where $e_a = \begin{bmatrix}e_1 \\ e_2\end{bmatrix}$ and $A_1 = \begin{bmatrix}-k_1 & 1 \\ -1 & -k_2\end{bmatrix}$ is Hurwitz matrix.

By adding and subtracting $\left(\frac{1}{4m\beta}e_F^2\right)$, the derivative of V_a can be expressed by

$$\dot{V}_a(e) = -e_a^T Q_a e_a - \frac{\beta}{m}\left(e_2 - \frac{1}{2\beta}e_F\right)^2 + \frac{1}{4m\beta}e_F^2, \tag{24}$$

Since $\left(e_2 - \frac{1}{2\beta}e_F\right)^2 > 0$, we can conclude that

$$\dot{V}_a(e) \leq -\lambda_{\min}(Q_a)\|e_a\|^2 + \frac{1}{4m\beta}\|e_F\|^2, \tag{25}$$

where $\|e_F\|$ is the bound of the force error using the feedforward controller. Thus, it can be shown that $\dot{V}_a$ is negative as $\dot{V}_a(e) \leq -\frac{1}{2}\lambda_{\min}(Q_a)\|e_a\|^2$, for $\|e_a\| > \frac{\|e_F\|}{\sqrt{2m\lambda_{\min}(Q_a)\beta}}$.

Since $\|e_F\|$ is bounded, then it can be concluded that $\dot{V}_a$ is a negative outside the compact residual set $\mathcal{R} = \left\{e_a : |e_a| \leq \frac{\|e_F\|_\infty}{\sqrt{2m\lambda_{\min}(Q_a)\beta}}\right\}$.

According to the definition of the Lyapunov function V_a in (21) and following the global boundedness analysis by [21], it can be concluded that $|e_a(t)|$ decreases whenever $e_a(t)$ outside the set $\mathcal{R}$, and hence $e_k(t)$ is asymptotic stable

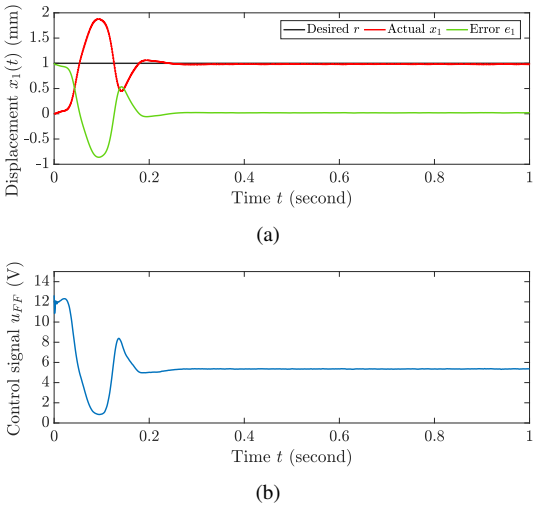

Fig. 9: Step response of the RAMS using the proposed control approach (a) tracking performance of the displacement x_1 in mm; and (b) the control signal u_{FF} in V.

and bounded by

$$\|e_a\|_\infty \leq \max\left\{|e_a(0)|, \frac{\|e_F\|_\infty}{\sqrt{2m\lambda_{\min}(Q_a)\beta}}\right\}. \tag{26}$$

C. Experimental verification

The primary aim is to assess the effectiveness of this control strategy in stabilizing the system and attaining the desired motion profile. In Figure 9, the tracking performance is displayed in response to a constant desired reference signal of $r = 1$ mm. It is evident from Figure 9 that the tracking error is approximately 18 μm, and the applied voltage hovers around 6 V. Figures 10 and 11 depict the tracking performance when subjected to a desired reference signal $r(t) = 0.5\sin(2\pi ft) + 0.7$, with excitation frequencies of $f = 0.5$ Hz and $f = 1$ Hz, respectively. It is evident that the maximum error remains around 100μm, and the applied voltage remains below 7 V.

These experimental results affirm the efficacy of the proposed control approach, demonstrating the system's capability to achieve tracking performance with an error of less than 2% for constant reference signals and less than 10% for sinusoidal reference signals.

VI. Conclusion

This paper has presented the characterization and control of a low-energy reluctance-actuated motion system (RAMS) for precision motion applications. The motion stage is equipped with different compression elements to provide varying stiffness values for the system. Subsequently, we have presented an experimental study of the RAMS to illustrate its displacement-current characteristics under various air gaps and applied voltage conditions. These experimental findings have revealed a significant nonlinearity within the system. Furthermore, we have analyzed the system's frequency response under specific input currents at different air gap settings. This analysis has pinpointed the system's

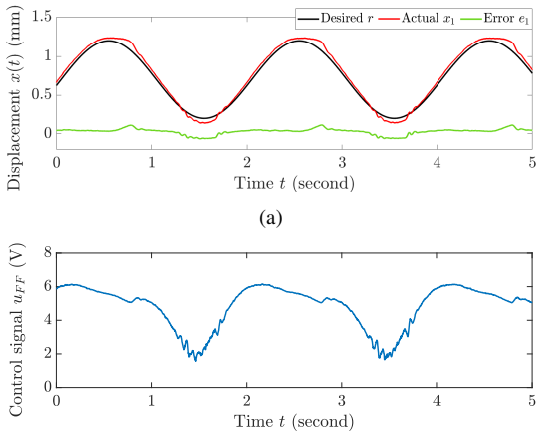

Fig. 10: Tracking performance to a desired sinusoidal motion profile as $r(t) = 0.5\sin(2\pi ft) + 0.7$ with frequency $f =$ 05 Hz (a) the displacement $x(t)$(mm); and (b) the control signal u_{FF} (V).

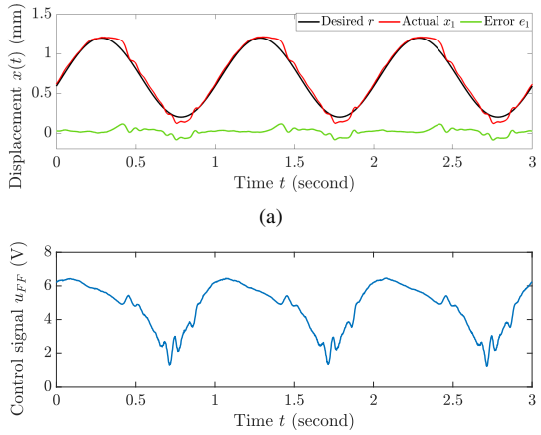

Fig. 11: Tracking performance to a desired sinusoidal motion profile as $r(t) = 0.5\sin(2\pi ft) + 0.7$ with frequency $f =$ 1 Hz (a) the displacement $x(t)$(mm); and (b) the control signal u_{FF} (V).

natural frequency, which has been determined to be $f_n =$ 25 Hz. To mitigate force errors arising from feedforward compensation, we have developed a state feedback controller based on the perturbation approach to achieve the desired motion profile. Experimental results have demonstrated the effectiveness of the proposed control approach in achieving tracking objectives, with errors of less than 2% for constant desired displacement and less than 10% when tracking a sinusoidal reference signal. Future work will focus on designing an advanced feedback control system to enhance tracking performance in both the time and frequency domains.

REFERENCES

[1] A. Katalenic, H. Butler, and P. Van Den Bosch, "High-precision force control of short-stroke reluctance actuators with an air gap observer," *IEEE/ASME Transactions on Mechatronics*, vol. 21, pp. 2431–2439, 2016.

[2] I. MacKenzie and D. Trumper, "Real-time hysteresis modeling of a reluctance actuator using a sheared-hysteresis-model observer," *IEEE/ASME Transactions on Mechatronics*, vol. 21, pp. 4–16, 2016.

[3] Y. Xu, X. Li, X. Yang, Z. Yang, L. Wu, and Q. Chen, "A two-stage model for rate-dependent inverse hysteresis in reluctance actuators," *Mechanical Systems and Signal Processing*, vol. 135, pp. 1–18, 2020.

[4] M. Al Saaideh, N. Alatawneh, and M. Al Janaideh, "Multi-objective optimization of a reluctance actuator for precision motion applications," *Journal of Magnetism and Magnetic Materials*, vol. 546, pp. 1–16, 2022.

[5] ——, "Design parameters of a reluctance actuation system for stable operation conditions with applications of high-precision motions in lithography machines," *IET Electric Power Applications*, vol. 16, no. 1, pp. 68–85, 2022.

[6] S. Ito, F. Cigarini, and G. Schitter, "Flux-controlled hybrid reluctance actuator for high-precision scanning motion," *IEEE Transactions on Industrial Electronics*, vol. 67, pp. 9593–9600, 2019.

[7] X. Zhang, L. Lai, and L. Zhu, "Data-driven fractional order phase-lead and proportional–integral feedback control strategy with application to a reluctance-actuated compliant micropositioning system," *Sensors and Actuators A: Physical*, vol. 348, pp. 1–11, 2022.

[8] X. Zhang, L. Lai, L. Zhang, and L. Zhu, "Hysteresis and magnetic flux leakage of long stroke micro/nanopositioning electromagnetic actuator based on maxwell normal stress," *Precision Engineering*, vol. 75, pp. 1–11, 2022.

[9] E. Csencsics, J. Schlarp, T. Schopf, and G. Schitter, "Compact high performance hybrid reluctance actuated fast steering mirror system," *Mechatronics*, vol. 62, pp. 1–10, 2019.

[10] E. Ramirez-Laboreo and C. Sagues, "Reluctance actuator characterization via fem simulations and experimental tests," *Mechatronics*, vol. 56, pp. 58–66, 2018.

[11] E. Moya-Lasheras, E. Ramirez-Laboreo, and C. Sagues, "Probability-based optimal control design for soft landing of short-stroke actuators," *IEEE Transactions on Control Systems Technology*, vol. 28, pp. 1956–1963, 2019.

[12] F. Cigarini, S. Ito, S. Troppmair, and G. Schitter, "Comparative finite element analysis of a voice coil actuator and a hybrid reluctance actuator," *IEEJ Journal of Industry Applications*, vol. 8, pp. 192–199, 2019.

[13] M. Al Saaideh, N. Alatawneh, K. Aljanaideh, and M. Al Janaideh, "Design and control of a reluctance-based micropositioning stage for scanning motion applications," in *2023 IEEE/RSJ International Conference on Intelligent Robots and Systems (IROS)*, 2023, pp. 2324–2329.

[14] M. Al Saaideh, A. M. Boker, and M. Al Janaideh, "Singular perturbation-based approach for robust control of reluctance-actuated motion systems," in *2023 62nd IEEE Conference on Decision and Control (CDC)*, 2023, pp. 8702–8707.

[15] S. Ito, S. Troppmair, B. Lindner, F. Cigarini, and G. Schitter, "Long-range fast nanopositioner using nonlinearities of hybrid reluctance actuator for energy efficiency," *IEEE Transactions on Industrial Electronics*, vol. 66, pp. 3051–3059, 2018.

[16] E. Csencsics, J. Schlarp, and G. Schitter, "High-performance hybrid-reluctance-force-based tip/tilt system: design, control, and evaluation," *IEEE/ASME Transactions on Mechatronics*, vol. 23, pp. 2494–2502, 2018.

[17] S. Ito, F. Cigarini, and G. Schitter, "Flux-controlled hybrid reluctance actuator for high-precision scanning motion," *IEEE Transactions on Industrial Electronics*, vol. 67, pp. 9593–9600, 2020.

[18] G. Stadler, E. Csencsics, S. Ito, and G. Schitter, "High precision hybrid reluctance actuator with integrated orientation independent zero power gravity compensation," *IEEE Transactions on Industrial Electronics*, vol. 69, pp. 13 296–13 304, 2021.

[19] X. Zhang, L. Lai, P. Li, and L. Zhu, "Data-driven fractional order feedback and model-less feedforward control of a XY reluctance-actuated micropositioning stage," *Review of Scientific Instruments*, vol. 93, pp. 1–16, 2022.

[20] M. Al Saaideh, A. M. Boker, and M. Al Janaideh, "Output-feedback control of electromagnetic actuated micropositioning system with uncertain nonlinearities and unknown gap variation," in *2022 IEEE 61st Conference on Decision and Control (CDC)*, 2022, pp. 2481–2486.

[21] M. Krstic, P. Kokotovic, and I. Kanellakopoulos, *Nonlinear and adaptive control design*. John Wiley & Sons, Inc., 1995.